OPEN ACCESS



The Impacts of Neutron Star Structure and Base Heating on Type I X-Ray Bursts and Code Comparison

Guoqing Zhen (甄国庆)¹, Guoliang Lü (吕国梁)^{2,1}, Helei Liu (刘荷蕾)¹, Akira Dohi (土肥明)^{3,4}, Nobuya Nishimura (西村信哉)^{5,6}, Chunhua Zhu (朱春花)¹, Liyu Song (宋利宇)¹, Weiyang Wang (王维扬)^{7,8}, and Renxin Xu (徐仁新)^{7,8}, school of Physical Science and Technology, Xinjiang University, Urumqi 830046, People's Republic of China; heleiliu@xju.edu.cn ² Xinjiang Astronomical Observatory, Chinese Academy of Science, 150 Science 1-Street, Urumqi 830011, People's Republic of China Department of Physics, Graduate School of Advanced Science and Engineering, Hiroshima University, Higashi-Hiroshima, Hiroshima 739-8526, Japan; dohiak@hiroshima.ac.jp

Interdisciplinary Theoretical and Mathematical Sciences Program (iTHEMS), RIKEN, Wako, Saitama 351-0198, Japan Satrophysical Big Bang Laboratory, Cluster for Pioneering Research, RIKEN, Wako, Saitama 351-0198, Japan RIKEN Nishina Center for Accelerator-Based Science, RIKEN, Wako, Saitama 351-0198, Japan Department of Astronomy, Peking University, Beijing 100871, People's Republic of China Kavli Institute for Astronomy and Astrophysics, Peking University, Beijing 100871, People's Republic of China Received 2023 January 17; revised 2023 April 13; accepted 2023 April 13; published 2023 June 14

Abstract

Type I X-ray bursts are rapidly brightening phenomena triggered by thermonuclear burning on the accreting layers of a neutron star (NS). The light curves represent the physical properties of NSs and the nuclear reactions on the proton-rich nuclei. The numerical treatments of the accreting NS and physics of the NS interior are not established, which shows uncertainty in modeling for observed X-ray light curves. In this study, we investigate theoretical X-ray burst models compared with burst light curves with GS 1826-24 observations. We focus on the impacts of the NS mass and radius and base heating on the NS surface using the MESA code. We find a monotonic correlation between the NS mass and the parameters of the light curve. The higher the mass, the longer the recurrence time and the greater the peak luminosity. While the larger the radius, the longer the recurrence time, the peak luminosity remains nearly constant. In the case of increasing base heating, both the recurrence time and peak luminosity decrease. We also examine the above results with a different numerical code, HERES, based on general relativity and consider the central NS. We find that the burst rate, energy, and strength are almost the same in two X-ray burst codes by adjusting the base heat parameter in MESA (the relative errors ≤5%), while the duration and rise times are significantly different between (the relative error is possibly ∼50%). The peak luminosity and the e-folding time change irregularly between two codes for different accretion rates.

Unified Astronomy Thesaurus concepts: X-ray bursts (1814); Neutron stars (1108); Nuclear abundances (1128); Accretion (14)

1. Introduction

Type I X-ray bursts are periodic eruptions caused by unstable thermonuclear burning on the surface of neutron stars (NSs) in low-mass X-ray binary systems (Joss 1977; Parikh et al. 2013). The NS accreted matter from the companion star overflowed through the Roche lobe and formed an envelope on the surface of the NS. Under the action of gravity, the accreted matter was continuously compressed and heated, thereby increasing the temperature and density; when the energy generation rate is greater than the cooling rate, thermonuclear unstable combustion will occur, resulting in type I X-ray bursts (Woosley & Taam 1976; Lewin et al. 1993; Bildsten 2000; Galloway & Keek 2021). The accreted matter mainly provides energy for type I X-ray bursts through the 3α reaction, CNO cycle, rp-process, etc. (Wallace & Woosley 1981; Taam 1985; Bildsten 1998; Galloway et al. 2008). Burning produces a heavy accumulation of ash, and as new material continues to pile on top of it, the accreted material undergoes gradual compression until it reaches a condition for ignition, producing another burst sequence.

Original content from this work may be used under the terms of the Creative Commons Attribution 4.0 licence. Any further distribution of this work must maintain attribution to the author(s) and the title of the work, journal citation and DOI.

Since the first discovery of the X-ray burst in 1975 (Belian et al. 1976; Grindlay et al. 1976), more than 7000 events from 1189 bursting sources have been observed so far (Galloway 2020). By comparing with observations, theoretical models can be calibrated, and the physical properties of NSs can be constrained (Cromartie et al. 2020). One of the preferred sources is GS 1826-24, because of its nearly uniform accretion rate and regular burst behavior, which is called a "clock" or "textbook" burst (Ubertini et al. 1999; Bildsten 2000). The X-ray burst models require input parameters regarding the accreted fuel composition (X, Y, Z), mass accretion rate (\dot{M}) , base heating (O_b) , and mass (M) and radius (R) of the NS, as well as nuclear reaction rates. Heger et al. (2007) studied the effect of metallicity (Z) and mass accretion rate on the theoretical light curves; by comparison with the light curve of GS 1826-24, they estimated the initial metallicity and accretion rate of GS 1826-24. Meisel (2018) investigated the sensitivity of models to varied accretion rates, base heating, metallicity, and the nuclear reaction rate $^{15}O(\alpha, \gamma)^{19}Ne$; with model-observation comparisons, they constrained the shallow heating in GS 1826-24 to be below $0.5 \,\mathrm{MeV}\,\mathrm{u}^{-1}$. The influence of nuclear reaction rate uncertainties on NS properties has also been studied from X-ray burst model—observation comparisons (Meisel et al. 2019).

https://personal.sron.nl/~jeanz/bursterlist.html

The above X-ray burst simulations are based on KEPLER (Heger et al. 2007) or MESA (Meisel 2018; Meisel et al. 2019), which consider the NS envelope using inner boundary conditions with a fixed NS mass and radius (1.4 M_{\odot} and 11.2 km). The effects of the NS mass and radius on thermonuclear flashes were investigated by Joss & Li (1980) and Ayasli & Joss (1982) using the stellar evolution code ASTRA. They adopted $M=1.4~M_{\odot}$ and $R=6.57~{\rm km}$ as a standard case and varied the mass to $M=0.705~M_{\odot}$ as the low-mass case and the radius to $R=13.14~{\rm km}$ as the large-radius case. The results show that the recurrence time, accumulated mass, burst energy, burst strength, and peak luminosity have obvious change. However, the results are not consistent with the recent NS mass-radius constraint (Steiner et al. 2010; Abbott et al. 2018).

Recently, Dohi et al. (2020, 2021, 2022) studied X-ray bursts using a general relativistic stellar evolution code with several NS equations of state (EOSs). They focused on the microphysics inside NSs (e.g., the mass and radius with different EOSs and the NS cooling process). By comparing with the burst parameters of GS 1826-24, they constrained the EOS and the NS mass and radius. Meanwhile, Johnston et al. (2020) applied Markov Chain Monte Carlo (MCMC) methods to 3840 KEPLER X-ray burst models and obtained system parameter estimates for GS 1826-24. They estimated a metallicity of $Z_{\rm CNO} = 0.010^{+0.005}_{-0.004}$, hydrogen fraction of $X_0 = 0.74^{+0.02}_{-0.03}$, mass $M > 1.7~M_{\odot}$, radius $R = 11.3^{+1.3}_{-1.3}$, etc. So far, the NS mass and radius are unknown for burst sources, but the mass and radius change the burst properties. It is worthwhile for us to extract the information on the macroscopic properties of NSs from the observation of X-ray bursts.

As X-ray burst simulations with a general relativistic stellar evolution code solve the stellar evolution equations from the center to the surface with the EOS, neutrino emission, crust heating, and nuclear energy generation in accreting layers are important for the comparison to X-ray burst observations (Dohi et al. 2020, 2021, 2022). The MESA and KEPLER codes only consider the accreting layers above the NS's solid crust, where the base heating parameter $Q_{\rm b}$ is adopted at the inner boundary to mimic the energy transfer from the NS interior. However, the value of the base heating is not well constrained by observation. Keek & Heger (2016) assumed $Q_b =$ 0.1 MeV u⁻¹. The deep crust heating theory suggests that the generated heat may be larger, up to $Q_b = 2 \text{ MeV u}^{-1}$ (Haensel & Zdunik 1990; Haensel 2003, 2008); although most of the heating in the deep crust is conducted into the core and carried off by neutrinos, a considerable amount of local heating will occur, which may increase Q_b . A yet-unknown shallow heating may also increase Q_b (Brown & Cumming 2009; Deibel et al. 2015; Lu et al. 2022). On the other hand, Q_b may be reduced by the competing effect of neutrino cooling (Cumming & Macbeth 2006); the Urca neutrino cooling process in the outer crust may also complicate the estimation of $Q_{\rm b}$ (Schatz et al. 2014). Thus, it is significant for us to study the effect of Q_b on X-ray bursts; with model—observation comparison, we may get a constraint on its value.

In addition, in Newtonian codes such as MESA or KEPLER, to accurately model bursts, it is important to account for the general relativity (GR) effects when comparing models with observations. The MESA code adopts the post-Newtonian correction to include the effects of GR (Paxton et al. 2015; Meisel 2018). The KEPLER code uses Newtonian gravity and

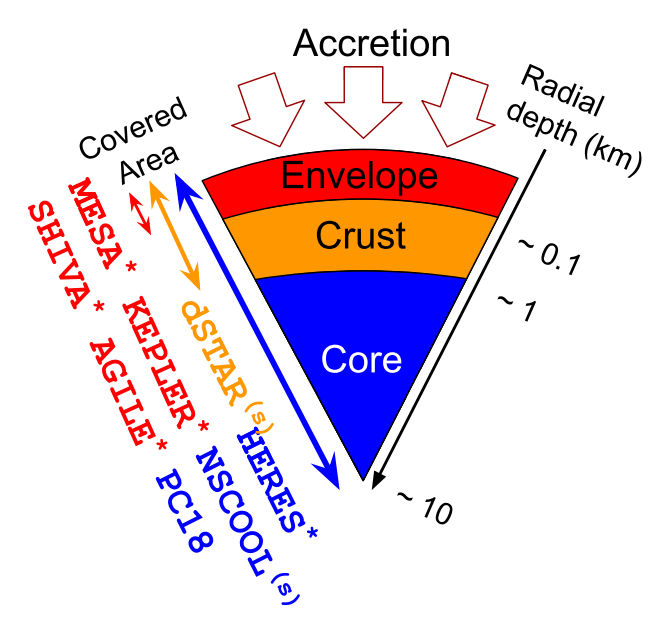


Figure 1. Schematic picture of the NS structure. The computational domain of several X-ray burst codes for the thermal evolution of accreting NSs is shown. The label with the asterisk considers the effects of convection and nuclear reaction networks, and the label with (s) treats the envelope as in the steady state.

ignores the GR effects; thus, GR corrections are adopted in X-ray burst simulations (Keek & Heger 2011; Johnston et al. 2018, 2020). In the present study, we adopt the MESA code to simulate a sequence of X-ray bursts and compare the results from a general relativistic stellar evolution code, HERES (Dohi et al. 2021), focusing on the burst observables.

The structure of the paper is as follows. In Section 2, we describe the post-Newtonian hydrodynamic MESA model and the GR hydrostatic HERES model. In Section 3, we present the results of computations wherein the effects of masses, radii, and base heating upon the X-ray burst properties are taken into account, and we compare the results from the MESA and HERES codes (Dohi et al. 2021) in Section 4. Finally, we summarize our results and briefly discuss their implications.

2. Model

There are several X-ray burst models that have different features due to the nature of the burst code. In Figure 1, we show a schematic of the NS structure and several corresponding burst codes. In several stellar evolutionary models, the most used code is the MESA code (Paxton et al. 2011, 2013, 2015, 2018), which solves the (post-)Newtonian hydrodynamics within the accreted regions. The formulation of MESA is quite similar to some codes of KEPLER (Woosley et al. 2004) and SHIVA (José & Hernanz 1998; José et al. 2010). These codes can be accessible even with the thermal evolution of relativistic compact objects by using the "GR correction" (e.g., Keek & Heger 2011), 10 but since the boundary condition on the crust surface is inevitably introduced as the " Q_b " value, it is hard for them to probe the NS physics. The approximate treatment of strong gravity in NSs as above may not be valid except for the surface; therefore, consistent treatment based on general relativistic formulation is indispensable for a more exact calculation of burst light curves.

 $[\]overline{^{10}}$ However, one of similar burst codes, AGILE (Liebendörfer et al. 2002; Fisker 2005), is based on GR.

The sophisticated public code that takes the above into account is the dSTAR code (Brown 2015), originally developed by Brown (2000). It simultaneously solves the Tolman–Oppenheimer–Volkoff (TOV) and energy transport equations without convection and reaction networks for X-ray bursts. It covers the regions except for the NS core and can probe the crust physics, such as crustal heating, shallow heating, Urca cooling, and so on (Deibel et al. 2015, 2016, 2017; Meisel & Deibel 2017). For the envelope, it treats it as in the steady state, which can construct a relation between surface temperature and crust temperature at the shallowest point (Brown et al. 2002). Still, dSTAR leaves the boundary condition on the core surface, which must be changed by the NS physics, such as the EOS and ν cooling effects.

To include more possible NS physics, we have recently developed the code HERES 11 (Dohi et al. 2020). HERES is essentially the same as dSTAR in that both follow the quasithermal evolution of accreting NSs, but the covered regions for calculation are extended to the center of the NSs. Unlike the other codes, no artificial boundary condition such as Q_b is required. Two other codes, NSCool (Colpi et al. 2001; Page & Reddy 2013) 12 and PC18 (Potekhin & Chabrier 2018; 13 see also Potekhin & Chabrier 2021), are similar to HERES in regard to the formulation but without a convection and reaction network for X-ray bursts. Therefore, HERES is currently the unique code that can probe the NS physics from X-ray burst light curves. In this work, we adopt the two distinct codes of MESA and HERES. Next, we briefly explain the properties of each code.

2.1. Post-Newtonian Hydrodynamic Model with Large Reaction Network (MESA)

We use an open-source stellar evolution code (MESA, version 9793; Paxton et al. 2015) to perform calculations on type I X-ray bursts. The MESA EOS is based on the 2005 OPAL EOS tables (Rogers & Nayfonov 2002); in addition, the SCVH tables (Saumon et al. 1995) and HELM (Timmes & Swesty 2000) and PC (Potekhin & Chabrier 2010) EOSs are employed for various conditions (Paxton et al. 2011). It is worth mentioning that a new Skye EOS for fully ionized matter was designed by Jermyn et al. (2021) and has been tested in action in the MESA stellar evolution code by computing white dwarf cooling curves. OPAL opacity tables are used with the protosolar abundances from Asplund et al. (2009). Following the approach described in Meisel (2018), we model a series of NS envelopes by considering inner boundary conditions for different NS masses and radii. The most pertinent details are repeated here. The luminosity at the base of the envelope is set to $L_{\text{base}} = \dot{M}Q_{\text{b}}$, where Q_{b} is the base heat, a parameter adopted by many models to simulate the heat flow from the NS's crust into the envelope (Brown & Cumming 2009; Keek & Heger 2017; Galloway & Keek 2021). The mass, radius, and base luminosity can be changed by using the commands relax M center, relax R center, and relax L center, respectively (Paxton et al. 2011). The GR effects were accounted for using a post-Newtonian modification to the local gravity (Paxton et al. 2011, 2015), where the MESA setting $use_GR_factors = .true$. was chosen. The envelope thickness is approximately $0.01\,\mathrm{km}$, and the initial metal abundance uses the solar metal abundance $Z=0.01,\ 0.02$ (Grevesse & Sauval 1998). We use the rp.net, which contains 304 isotopes (see Lund Fisker et al. 2007), and the nuclear reaction rates use the reaction rates from the REACLIB V2.2 library (Cyburt et al. 2010). Adaptive time and spatial resolution were employed according to the MESA controls $varcontrol_target=1d-3$ and $mesh_delta_coeff=1.0$ (Paxton et al. 2013). In order to achieve convergent solutions, some models need slightly different settings. In Table 1 from the Appendix, we provide our burst models, which describe the input parameters and some of the outputs in more detail.

2.2. General Relativistic Hydrostatic Evolutional Model with an Approximate Reaction Network (HERES)

As explained above, MESA has two issues with the treatment of the NS gravity and artificial boundary conditions introduced as Q_b . The definitions of Q_b are different in previous works; e.g., Q_b is defined by Keek & Heger (2016) to mean the amount of heat generated by crustal heating at the base of the envelope, and the typical value for Q_b of $0.1 \,\mathrm{MeV}\,\mathrm{u}^{-1}$ was adopted. Meisel (2018) defined Q_b to mean not only the crust heating but also the shallow heating. To mimic the shallow heating of unknown origin, $Q_b = 0.1$, 0.5, and 1.0 MeV u⁻¹ were adopted. Hereafter, we define the net base heat as $Q_{\rm e}$, which represents the energy exchange between the interior NS and the accreting layer; its value could be changed by the unknown shallow heating or the ν cooling processes inside NSs related to the EOS and mass (see Table 2 in Dohi et al. 2021). In such a formulation, it is principally impossible to treat the heat flux coming from the interior of NSs, which drastically changes the overall temperature through electron (and radiative) thermal conductivity. Thus, we should validate the MESA burst models in particular for the physical effects inside NSs.

As the most realistic burst model that covers entire NS regions, we utilize some of the ones presented by Dohi et al. (2021), who followed quasi-hydrostatic evolution by using HERES. We take an approximate reaction network with 88 isotopes for mixed hydrogen and helium burning (APRX3 in Dohi et al. 2020) and the same data of reaction rates as MESA. In the energy transport equation, we implement the Schwarzschild convection. Note that convection is required for causing the mixed hydrogen/helium burning, though it is somewhat artificial due to a one-dimensional formulation. The initial models for our X-ray burst calculation are set to be the steadystate models (Liu & Dohi 2021) with gravitational compressional heating (see Matsuo et al. 2018 for details).

Let us explain the model parameters in HERES. The accretion rates and compositions of accreted matter are the same as in Section 2.1. We utilize the nuclear EOS of Togashi, which is based on the variational approach with the use of the bare nuclear potentials for two-body interaction and phenomenological three-body interaction (Togashi et al. 2017). For the heating source, the standard crustal heating rates of Haensel & Zdunik (1990) are implemented. For the cooling source, we consider the slow ν cooling processes mainly composed of the modified Urca process and bremsstrahlung. The occurrence of

¹¹ The name derives from "One-Dimensional Hydrostatic Evolution of RElativistic Stars." Our code originally derives from Fujimoto et al. (1984).

 $^{^{12}}$ Updated code for accreting NSs from the original one (Page 1989). The envelope is treated in steady state.

 $^{^{13}}$ Note that the effects of the magnetic field in NSs are considered, unlike other codes.

 $[\]overline{^{14}}$ Regarding 64 Ge(p, γ) 65 As and 65 As(p, γ) 66 Se, Dohi et al. (2021) adopted the data from Lam et al. (2016). In this paper, however, we remake the HERES burst models with the reaction rates of Cyburt et al. (2016), which are implemented in MESA.

fast ν cooling processes such as the nucleon direct Urca process, i.e., neutrino emissions induced by (inverse) β decay, could affect the burst light curves (Dohi et al. 2022), but for any mass, it is prohibited with the Togashi EOS due to the quite low symmetry energy (the slope parameter L is 30 MeV; Dohi & Nakazato 2019).

3. The Impact of NS Mass, Radius, and Base Heating on Type I X-Ray Bursts

We build a series of scenarios (models 1–12 in Table 1) with variations in mass (models 1–4), radius (models 5–8), and base heating (models 9–12), then type I X-ray bursts on the surface layer of accreting NSs are simulated using MESA with the above inputs.

The light curves of the X-ray bursts are usually characterized by several parameters, e.g., the recurrence time Δt , which represents the time from one burst to the next. The burst duration τ is defined to be the time after the peak at a half value of $L_{\rm peak}$. The rise time $t_{\rm rise}$ is defined from transience to the peak point. The e-folding time $\tau_{\rm e}$ is defined after the peak point. The peak luminosity $L_{\rm peak}$ is taken from the light-curve maximum. The burst energy E_b is obtained by integrating over the light curve

$$E_b = \int L_b dt. \tag{1}$$

The burst strength α is defined by the ratio of the accretion energy to the burst energy,

$$\alpha = \frac{z_g}{1 + z_g} \dot{M}c^2 \frac{\Delta t}{E_b},\tag{2}$$

where z_g is the gravitational redshift.

In order to compare with observations, we stack a sequence of bursts from each model and obtain the average light curve, burst parameters, and 1σ error for them. Since the wait time for the next burst is usually shortened as the ash from the previous burst is mixed with the new fuel, i.e., compositional inertia (Taam 1980; Woosley et al. 2004), we remove the data of the first four bursts and start processing from the fifth burst. The convergence of MESA light curves is almost archived at \sim five bursts, which is fewer than the \sim 10 bursts in KEPLER without nuclear preheating (see Figure A1 in Johnston et al. 2020). ¹⁵

3.1. Variations in NS Mass, Radius, and Base Heating and X-Ray Burst Parameters

The X-ray bursts with various values of NS mass, radius, and base heating are calculated. In the left panel of Figure 2, we show the luminosity of the burst sequence with different NS mass models. We calculate the averaged light curves by aligning bursts in each sequence by their peak luminosities, and the results are shown in the right panel. Similarly, the luminosity of the burst sequence with different NS radius models is shown in the left panel of Figure 3, and the averaged light curves are shown in the right panel. We find that with the increase of mass, $L_{\rm peak}$ increases, Δt increases, and decay time decreases. However, as the radius is increased, Δt also increases, $L_{\rm peak}$ remains constant, and decay time increases.

The results for different base heating cases are shown in Figure 4; as $Q_{\rm e}$ is increased, $L_{\rm peak}$ decreases, Δt decreases, and decay time decreases. In the following, we calculate burst parameters such as Δt , $L_{\rm peak}$, α , $E_{\rm burst}$, $t_{\rm rise}$, τ , and $\tau_{\rm e}$, and one can find the values in detail in Table 1. Meanwhile, the ignition pressure $P_{\rm ign}$ for each model is obtained to understand the variation of parameters.

The parameter changes with variations in mass, radius, and base heating are shown in Figure 5. For models 1–4 in Table 1 (left panel in Figure 5), as M increases, Δt , α , $L_{\rm peak}$, $E_{\rm b}$, and $P_{\rm ign}$ increase. For a fixed NS radius, M increases, and the surface gravitational acceleration ($g_{\rm s}$) becomes larger, resulting in an increase in ignition pressure($P_{\rm ign}$). One can also find the ignition pressure from the bottom panel in Figure 5, which is increased when the mass increases. According to the one-zone model, the column density σ is expressed in two ways (Bildsten 1998; Dohi et al. 2022),

$$\sigma = \frac{\dot{M} \times \Delta t}{4\pi R^2} = P_{\rm ign} / g_{\rm s},\tag{3}$$

where $g_{\rm s}=\frac{GM}{R^2}\Big(1-\frac{2GM}{Rc^2}\Big)^{-1/2}$, and one can see the surface gravity acceleration $g_{\rm s}$ on the mass–radius plane in detail from Figure 3 of Dohi et al. (2021). As a result, for the fixed accretion rate and NS radius, with increasing mass, the recurrence time is proportional to $P_{\rm ign}/g_{\rm s}$. The increase of ignition pressure overtakes the increase of surface gravity acceleration, which leads to the increase of Δt . The peak luminosity can be scaled as the Eddington limit (Lewin et al. 1993),

$$L_{\rm peak} \sim L_{\rm Edd} = 4\pi c G M/\kappa \propto M,$$
 (4)

which is proportional to M but independent of R, where κ is the electron scattering opacity. Therefore, the peak luminosity is increased when M increases.

Assuming that all accreted matter is processed in flashes, the burst strength is the ratio of the average luminosity emitted in the persistent X-ray emission (L_p) to that emitted in X-ray bursts (L_b ; Lewin et al. 1993),

$$\alpha = \frac{L_{\rm p}}{L_{\rm b}} = \frac{\varepsilon_{\rm G}}{\varepsilon_{\rm N}} \sim (25-100) \frac{M/M_{\odot}}{R/10 \,\rm km},\tag{5}$$

where $\varepsilon_G = GM/R$ is the gravitational energy release per gram, and ε_N is the nuclear energy. According to Equation (5), for a fixed NS radius, α increases as mass increases. Our results from the MESA simulation are almost consistent with the above simple one-zone model assumption.

The middle panel of Figure 5 shows that the $P_{\rm ign}$ and α of the bursts are inversely proportional to the radius, and Δt and $E_{\rm b}$ are proportional to the radius, while the peak luminosity $L_{\rm peak}$ remains constant. As the radius increases, the gravitational acceleration on the surface of the NS becomes smaller, and the ignition pressure decrease Δt is longer due to the increased NS surface area. The burst energy is larger due to the longer e-folding time. The burst strength α is reduced due to the lower surface gravitational potential, which also can be easily understood from Equation (5). According to Equation (4), as the peak luminosity does not depend on radius, the peak luminosity is almost constant as radius increases.

¹⁵The HERES light curves are converged around 10–30 burst times, which is more than those in MESA and KEPLER. This is because HERES adopts the anisothermal structure as the initial model (Matsuo et al. 2018), which spends the convergence time due to the existence of thermal flux.

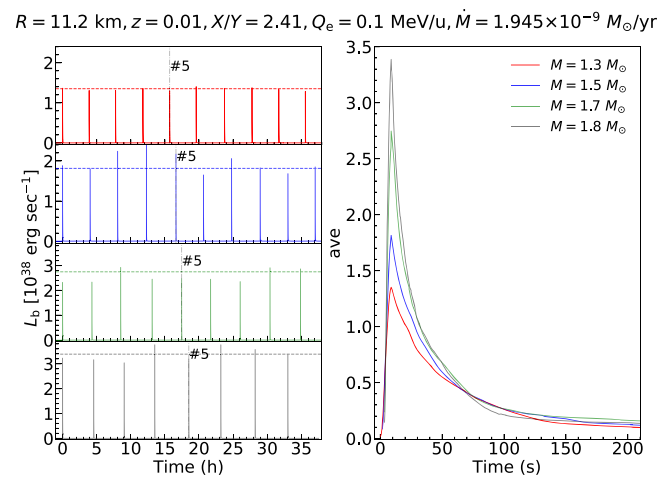


Figure 2. Light curves with different mass models. Left: luminosity of the burst sequence during 0–40 hr with different NS mass models, i.e., 1.3 (red), 1.5 (blue), 1.7 (green), and 1.8 (black) M_{\odot} . The horizontal dashed line in each panel represents the average peak luminosity. Right: average light curves.

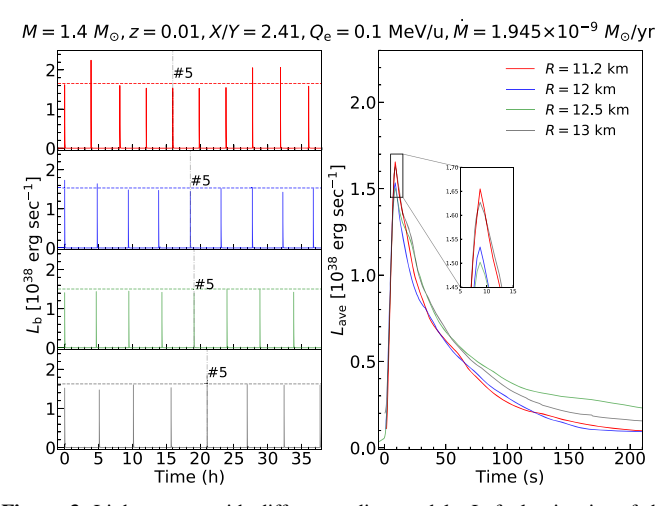


Figure 3. Light curves with different radius models. Left: luminosity of the burst sequence during 0–40 hr with different NS radius models; i.e., 11.2 (red), 12 (blue), 12.5 (green), and 13 (black) km. The horizontal dashed line in each panel represents the mean peak luminosity. Right: average light curves.

The results for the parameter variation with base heating are shown in the right panel of Figure 5. With the increase of $Q_{\rm e}$, the peak luminosity of the burst decreases continuously, and the interval between bursts becomes smaller. This is because the first hot CNO cycle, i.e., $^{12}{\rm C}(p,\,\gamma)^{13}{\rm N}(p,\,\gamma)^{14}{\rm O}(\beta^+)^{14}{\rm N}(p,\,\gamma)^{15}{\rm O}(\beta^+)^{15}{\rm N}(p,\,\alpha)^{12}{\rm C}$, lasts longer with smaller $Q_{\rm e}$. The timescale of the hot CNO cycle is almost determined by the abundances of $^{14}{\rm O}$ and $^{15}{\rm O}$, which could trigger new $(\alpha,\,p)$ reaction paths, indirectly leading to proton-rich nucleosynthesis. If $Q_{\rm e}$ is smaller (in the range of 0 MeV ${\rm u}^{-1} < Q_{\rm e} < 0.5\,{\rm MeV}\,{\rm u}^{-1}$), i.e., the interior NS is colder, excessive protons turn into helium, which burns to $^{12}{\rm C}$ by the 3α reaction at faster rates because it takes more time to accumulate the seeds, $^{14}{\rm O}$ and $^{15}{\rm O}$, leading to higher Δt . Then,

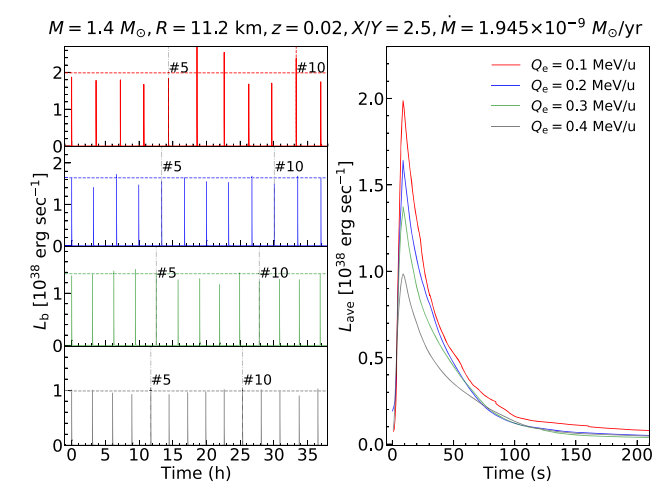


Figure 4. Light curves with different Q_e . Left: luminosity of the burst sequence during 0–40 hr with different Q_e , i.e., 0.1 (red), 0.2 (blue), 0.3 (green), and 0.4 (black) MeV u⁻¹. The horizontal dashed line in each panel represents the mean peak luminosity. Right: average light curves.

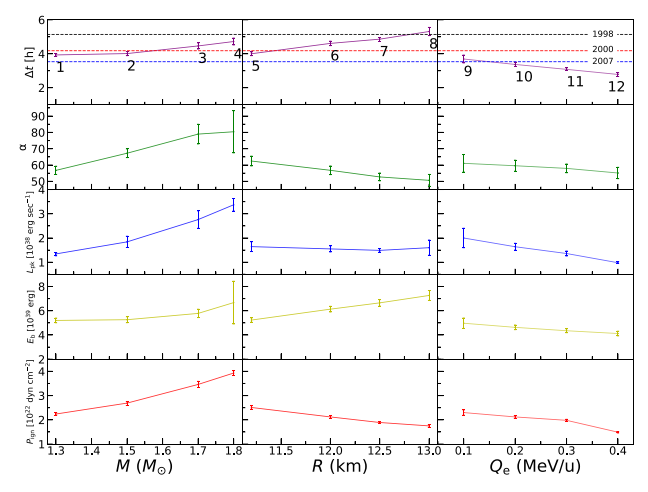


Figure 5. Values of Δt , α , $L_{\rm peak}$, $E_{\rm b}$, and $P_{\rm ign}$ with different M (left), R (middle), and $Q_{\rm e}$ (right). The dashed lines in the uppermost panels indicate the recurrence time from observations. The numbers 1–12 in the uppermost panels indicate the model number, which is shown in Table 1 from the Appendix.

the e-folding time tends to be shorter because the protons that are the critical fuel of the rp-process are more exhausted. As a result, more energy is produced during the hot CNO cycle due to its longer duration if $Q_{\rm e}$ is smaller, leading to a higher peak luminosity. We note that the $Q_{\rm e}$ dependence of the hot CNO cycle timescale is, in a sense, similar to the $^{15}{\rm O}(\alpha,\gamma)^{19}{\rm Ne}$ rate dependence of that, which was studied by Fisker et al. (2006, 2007).

3.2. Model-Observation Comparisons

The light curves with variations in NS mass, radius, and base heating are compared with observations in Figure 6, where the observed light curve of GS 1826-24 in 2007 is adopted. We include the burst anisotropy ξ_b in the distance, and $d\xi_b^{1/2}$ is calculated from $F_{\rm peak} = L_{\rm peak}/4\pi d^2\xi_b$. With use of the χ^2 method in Dohi et al. (2020), we can get the best-fit $d\xi_b^{1/2}$ for each model–observation comparison. From the left panels of

¹⁶ At a low temperature of $T\lesssim 4\times 10^8$ K, β decays are dominant, but at high temperatures, the second hot CNO cycle, ¹⁴O(α , p)¹⁷F(p, γ)¹⁸Ne(β ⁺)¹⁸F(p, α)¹⁵O, occurs instead of ¹⁴O(β ⁺). The resultant breakout reactions to α p- and rp-processes are therefore ¹⁵O(α , γ)¹⁹Ne and ¹⁸Ne(α , p)²¹Na.

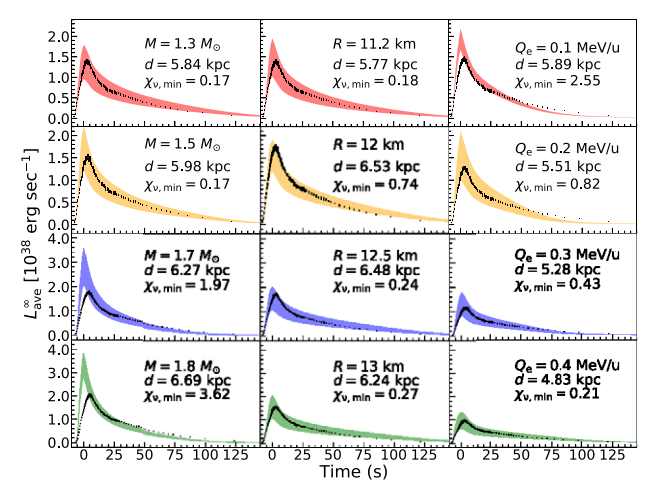


Figure 6. Comparison of the calculated averaged burst light curves with 1σ error regions (M=1.3, 1.5, 1.7, and $1.8 M_{\odot}$; R=11.2, 12, 12.5, and 13 km; and $Q_{\rm e}=0.1, 0.2, 0.3,$ and 0.4 MeV u⁻¹) with the observed ones of GS 1826-24 in 2007.

Figure 6, we can see that the peak luminosity increases as mass increases, and the peak luminosity is too high to fit the observation for $M \ge 1.7 M_{\odot}$. In the middle panels of Figure 6, the peak luminosity is almost constant as the radius increases, and the light curve can be well fitted with a radius in the range of $\sim 11.2-13$ km. In the right panels of Figure 6, the peak luminosity decreases as base heating increases, and the light curve can be well fitted with the variation of base heating in the range $Q_e = 0.1-0.4 \text{ MeV u}^{-1}$. Besides, we also compare the recurrence time with observations in the uppermost panels of Figure 5. The burst models of 1–10 are consistent with the observed values. The recurrence time is too short to interpret observations for burst models 11 and 12 with $Q_e = 0.3$ and 0.4 MeV u⁻¹. However, the source distance is uncertain, which is crucial to determine the shape of the light curve. The input parameters, such as metallicity and accretion rate, also affect the burst light curve. It is better for us to use the MCMC method (e.g., Johnston et al. 2020) to determine the system parameters. In our calculation, models 9 and 10 are consistent with the observation of GS 1826-24 in 2007 (whether the light curve or the recurrence time).

4. Code Comparison

In order to validate the models for X-ray burst calculation such as MESA, which solves the Newtonian hydrodynamics with the accreted layers, we adopt the realistic code HERES, which solves the whole NS as a comparison. In Table 2 from the Appendix, we show our calculation models with the HERES code. By using an adopted mass, radius, and accretion rate under X/Y = 2.9 and $Z_{CNO} = 0.02$, we obtain several burst parameters, such as burst strength α , burst duration τ , recurrence time Δt , total burst energy E_{burst} , peak luminosity $L_{\rm peak}$, and rise time $t_{\rm rise}$. The 1σ errors are also presented for each output parameter. The base heating inferred from the 1.4 M_{\odot} NS with the Togashi EOS is $Q_{\rm e} = 0.35 \,{\rm MeV \, u^{-1}}$ (Dohi et al. 2021). The light curves calculated with the HERES code are shown in Figure 7. It shows that the recurrence time decreases as the accretion rate increases, with the peak luminosity almost constant. Meanwhile, we adopt the same mass, radius, metallicity, X/Y, base heating, and accretion rate

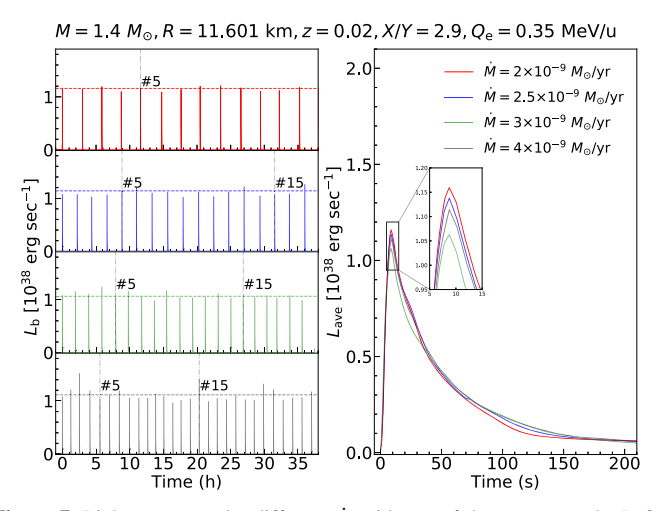


Figure 7. Light curves under different \dot{M} with use of the HERES code. Left: luminosity of the burst sequence during 0–40 hr for several \dot{M} . The horizontal dashed line in each panel represents the mean peak luminosity. Right: average light curves.

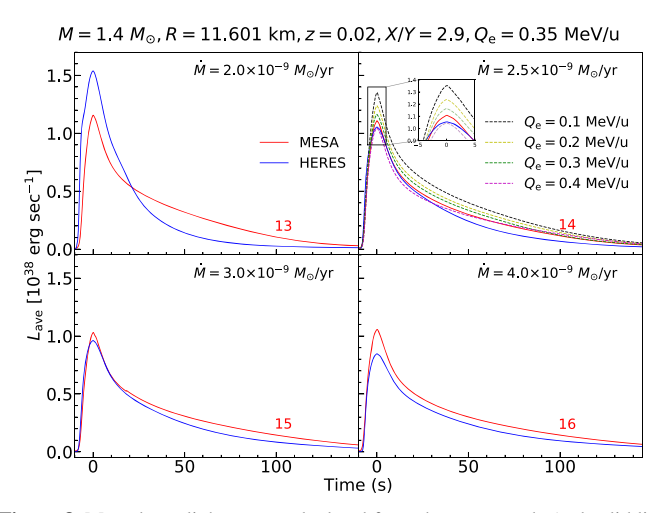


Figure 8. Mean burst light curve calculated from the MESA code (red solid line and model numbers 13–15 are marked in each panel) vs. the mean light curve calculated from the HERES code (blue solid line), where $Q_{\rm e}=0.35~{\rm MeV}~{\rm u}^{-1}$. In the upper right panel, the dashed lines in different colors (black, yellow, green, and purple) are the same as the red solid line but with different base heating (0.1, 0.2, 0.3, and 0.4 MeV ${\rm u}^{-1}$).

for the MESA X-ray burst calculations. The input parameters and some of the output parameters are shown in Table 1 from models 13-16 in the Appendix.

Figure 8 shows the comparison of the mean light curves between the MESA and HERES calculations. The difference between the two light curves is very small, with accretion rates of $\dot{M}=2.5\times 10^{-9}$ and $3.0\times 10^{-9}\,M_\odot$ yr⁻¹. There are big differences for peak luminosity and luminosity at the tail parts of the light curve between two codes under accretion rates of $\dot{M}=2.0\times 10^{-9}$ and $4.0\times 10^{-9}\,M_\odot$ yr⁻¹. The main difference is due to the higher hydrostatic force, i.e., higher compressional heating in HERES models (Matsuo et al. 2018), which leads to a higher peak luminosity than MESA. Note that the contribution of compressional heating to total luminosity ($\sim 10^{38}\,{\rm erg}\,{\rm s}^{-1}$) is around 10%. In Figure 9, we show the differences of the compressional heating luminosity

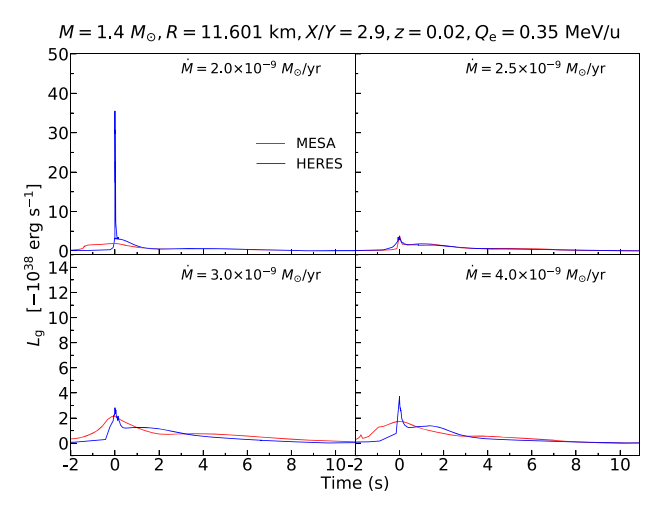


Figure 9. Comparison of the compressional heating luminosity $L_{\rm g}$ for the MESA (red) and HERES (blue) codes.

 $L_{\rm g}$ between the MESA and HERES codes with four different accretion rates. At a low accretion rate, $\dot{M}=2.0\times 10^{-9}\,M_{\odot}\,{\rm yr^{-1}}$, the peak luminosity of $L_{\rm g}$ obtained from the HERES code is much higher than that in the MESA code. For the rest of the accretion rates, the compressional heating luminosities are almost the same between the two codes. The difference due to reaction networks, i.e., nuclear burning energy rates and compositions, appears in the tail parts, where the luminosity is higher in MESA models regardless of \dot{M} .

Next, we also calculate models 17–20 with different base heating based on model 14 in the upper right panel of Figure 8. It shows that the lower the base heating, the higher the peak luminosity and the luminosity at the tail parts, which leads to a big deviation from the case with $Q_{\rm e}=0.35\,{\rm MeV\,u}^{-1}$.

Finally, we compared the predicted burst parameters (α , $E_{\rm b}$, Δt , $L_{\rm peak}$, $t_{\rm rise}$, and $\tau_{\rm e}$) of the two codes for a range of accretion rates in Figure 10. In both codes, the burst strength α , total burst energy $E_{\rm b}$, and recurrence time Δt are highly consistent. The differences of the peak luminosity and the tail parts of the light curve between the two codes are obvious (e.g., the maximum relative errors of t_{rise} and L_{peak} are about $\sim 50\%$). Thus, for the first time, the consistency of the two codes is identified by our comparison. The differences for the peak luminosity at the low accretion rate are caused by the high compressional heating luminosity as shown in Figure 9, while the high luminosity at the tail parts regardless of accretion rate is possibly caused by the nuclear reaction energy and compositions. The comparison of the nuclear reaction networks adopted in MESA (rp.net) and HERES (APRX3) is shown in Table 3. It is worth noting that our input values and the values of the burst parameters obtained from the MESA code, which adopts a post-Newtonian modification for GR effects, are unified to the local frame; in order to compare with the observations that were detected by a distant observer, the redshift of the parameters should be considered. In the Appendix, we show the detailed formulae to transfer the local frame quantities to the frame of a distant observer.

5. Conclusions

In this work, we present a set of simulations of X-ray bursts with variations in NS mass, radius, and base heating using the open-source code MESA. The light curves and burst parameters

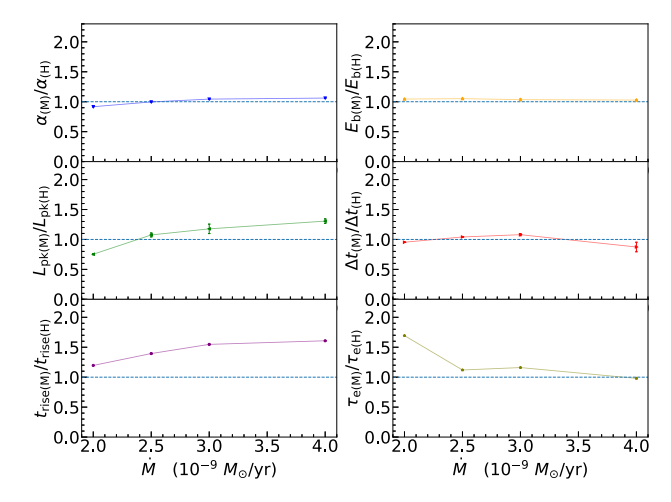


Figure 10. Comparison of the burst parameters $(\alpha, E_b, \Delta t, L_{peak}, t_{rise}, \text{ and } \tau_e)$ for the MESA and HERES codes for a range of accretion rates. Here "M" and "H" are marked in the subscript of each parameter to indicate that the results are obtained from MESA and HERES, respectively.

are obtained for each model. We find that the recurrence time, burst strength, peak luminosity, and total burst energy are increased as the mass increases. As the radius increases, the recurrence time and total burst energy increase, the burst strength decreases, and the peak luminosity remains constant. The recurrence time, burst strength, peak luminosity, and total burst energy decrease as base heating increases. The above phenomena can be well explained with the use of the simple one-zone model. One can see Section 3.1 for a detailed explanation.

The codes, such as KEPLER and MESA, solve the Newtonian hydrodynamics only within the accreted regions to simulate X-ray bursts. As a result, it is hard to probe the NS physics. HERES solves the TOV and energy transport equations; hence, it can include all possible physics. To assess the validity of the boundary condition on the crust and the GR correction for the Newtonian hydrodynamics calculations, we made a comparison between multizone burst models from the MESA and HERES codes for the first time. The results show that the average light curves are highly consistent under accretion rates of $\dot{M} = 2.5 \times 10^{-9}$ and $3.0 \times 10^{-9} \, M_{\odot} \, \mathrm{yr}^{-1}$, while under accretion rates $\dot{M}=2.0\times10^{-9}$ and $4.0\times10^{-9}\,M_{\odot}\,\mathrm{yr}^{-1}$, the peak luminosity and cooling tail are obviously different between the two codes. However, the burst strength, total burst energy, and recurrence time are consistent between the two codes regardless of accretion rate. It is worth noting that the light curves are inconsistent when we choose other values of O_e .

We demonstrate that the NS mass, radius, and base heating have a nonnegligible effect on the X-ray burst simulation. The validity of the boundary condition and GR correction for the MESA code is verified by the code comparison between MESA and HERES. The variation trend of the output parameters with different NS mass, radius, base heating, and accretion rate can help us to understand the properties of NSs via X-ray burst observations.

The difference in the X-ray burst codes appears in not only the light curves but also rp-process nucleosynthesis. In fact, Parikh et al. (2008) showed the differences in the final products among three burst models with postprocess calculation. A similar comparison with the use of MESA and HERES may also

give information on some model parameters and will be presented in the near future.

Acknowledgments

We appreciate the referee for valuable comments that improved this manuscript. We thank S. Nagataki and M. Hashimoto for their encouragement. This work received the generous support of the National Natural Science Foundation of China Nos. 12263006, U2031204, and 12163005; the Natural Science Foundation of Xinjiang Province under grant Nos. 2020D01C063 and 2021D01C075; and the Science Research Grants from the China Manned Space Project with No. CMS-CSST-2021-A10. A.D. is supported by a JSPS Research Fellowship for Young Scientists (22J10448). N.N. is supported by the JSPS KAKENHI (19H00693, 20H05648, 21H01087) and the RIKEN Intensive Research Project.

Appendix A Correcting the Quantities from the Local Frame to the Frame of a Distant Observer

To compare with observations, it is crucial to correct the GR quantities from the local reference frame of the NS surface to the frame of a distant observer, which we mark with the superscript " ∞ ." The timescale will be redshifted by

$$t^{\infty} = (1 + z_g)t, \tag{A1}$$

where
$$1 + z_g = \frac{1}{\sqrt{1 - \frac{2GM}{Rc^2}}}$$
.

The redshifted luminosity can be written as

$$L^{\infty} = \frac{L}{(1+z_{\sigma})^2}. (A2)$$

Because the burst energy E_b is obtained by integrating over the time (see Equation (1)), from Equations (A1) and (A2), the redshifted burst energy is given by

$$E_{\rm b}^{\infty} = \frac{E_{\rm b}}{1 + z_{\rm o}}.\tag{A3}$$

Similarly, the redshifted mass accretion rate is given by

$$\dot{M}^{\infty} = \frac{\dot{M}}{1 + z_{g}}.$$
 (A4)

The local burst strength from Equation (2) can be redshifted by

$$\alpha^{\infty} = \frac{\alpha}{1 + z_g}.$$
(A5)

One can transfer the timescales (e.g., recurrence time Δt , rise time $t_{\rm rise}$, duration time τ , and e-folding time $\tau_{\rm e}$), luminosities (e.g., peak luminosity $L_{\rm pk}$), burst energy $E_{\rm b}$, mass accretion rate \dot{M} , and burst strength α from the local reference frame to an observer frame with the above formulae.

Appendix B X-Ray Burst Models and Nuclear Reaction Networks

For convenience, we show the physical quantities of burst models for MESA and HERES codes in Table 1 and Table 2, respectively. The nuclear reaction network of rp.net and APRX3 is shown in Table 3.

Model Number	$M \over M_{\odot}$	R km	$Z_{ m CNO}$	$Q_{ m e}$ MeV $ m u^{-1}$	$10^{-9} \frac{\dot{M}}{M_{\odot}} \mathrm{yr}^{-1}$	${\rm MeV} {\rm u}^{-1}$	$E_{ m burst}$ $10^{39} { m erg}$	$L_{\rm peak}$ $10^{38} {\rm erg \ s}^{-1}$	Δt hr
1	1.3	11.2	0.01	0.1	1.945	56.70 ± 2.42	5.21 ± 0.19	1.34 ± 0.08	3.93 ± 0.11
2	1.5	11.2	0.01	0.1	1.945	67.24 ± 2.49	5.27 ± 0.25	1.81 ± 0.22	4.00 ± 0.12
3	1.7	11.2	0.01	0.1	1.945	79.31 ± 6.39	5.79 ± 0.35	2.73 ± 0.35	4.48 ± 0.18
4	1.8	11.2	0.01	0.1	1.945	85.30 ± 1.85	6.06 ± 0.30	3.37 ± 0.31	4.73 ± 0.24
5	1.4	11.2	0.01	0.1	1.945	62.54 ± 2.99	5.23 ± 0.18	1.65 ± 0.21	4.00 ± 0.11
6	1.4	12.0	0.01	0.1	1.945	56.30 ± 2.91	6.19 ± 0.23	1.54 ± 0.09	4.61 ± 0.47
7	1.4	12.5	0.01	0.1	1.945	52.76 ± 2.47	6.67 ± 0.26	1.50 ± 0.08	4.87 ± 0.12
8	1.4	13.0	0.01	0.1	1.945	50.77 ± 3.70	7.30 ± 0.41	1.62 ± 0.33	5.34 ± 0.23
9	1.4	11.2	0.02	0.1	1.945	61.05 ± 5.40	4.97 ± 0.43	2.00 ± 0.4	3.69 ± 0.24
10	1.4	11.2	0.02	0.2	1.945	59.57 ± 3.37	4.63 ± 0.19	1.64 ± 0.14	3.37 ± 0.12
11	1.4	11.2	0.02	0.3	1.945	57.95 ± 2.65	4.35 ± 0.16	1.36 ± 0.09	3.08 ± 0.09
12	1.4	11.2	0.02	0.4	1.945	55.12 ± 3.45	4.12 ± 0.19	0.98 ± 0.04	2.78 ± 0.10
13	1.4	11.601	0.02	0.35	2.0	52.51 ± 2.43	4.47 ± 0.16	1.16 ± 0.05	2.90 ± 0.08
14	1.4	11.601	0.02	0.35	2.5	52.93 ± 3.91	4.33 ± 0.27	1.14 ± 0.13	2.26 ± 0.11
15	1.4	11.601	0.02	0.35	3.0	55.04 ± 3.55	4.19 ± 0.40	1.13 ± 0.25	1.90 ± 0.13
16	1.4	11.601	0.02	0.35	4.0	55.28 ± 2.37	4.04 ± 0.26	1.11 ± 0.13	1.38 ± 0.09
17	1.4	11.601	0.02	0.1	2.5	57.92 ± 3.15	4.87 ± 0.22	1.36 ± 0.22	2.79 ± 0.08
18	1.4	11.601	0.02	0.2	2.5	55.99 ± 1.67	4.57 ± 0.14	1.24 ± 0.07	2.53 ± 0.08
19	1.4	11.601	0.02	0.3	2.5	54.50 ± 3.80	4.36 ± 0.25	1.17 ± 0.09	2.35 ± 0.13
20	1.4	11.601	0.02	0.4	2.5	53.35 ± 3.03	4.06 ± 0.21	1.05 ± 0.04	2.14 ± 0.12
Model			_	_					
	M	R	$Z_{\rm CNO}$	$Q_{ m e}$	\dot{M}	$t_{ m rise}$	au	$ au_{ m e}$	$P_{\rm ign}$
Number	$M \over M_{\odot}$	<i>R</i> km	Z_{CNO}	$Q_{ m e}$ MeV ${ m u}^{-1}$	$M = 10^{-9} M_{\odot} \text{ yr}^{-1}$	$t_{ m rise}$ s	aus	$ au_{ m e}$ s	$10^{22} \mathrm{dyn}\mathrm{cm}^{-2}$
			2 _{CNO}	$\frac{Q_{\rm e}}{\text{MeV u}^{-1}}$	$\frac{M}{10^{-9} M_{\odot} \text{ yr}^{-1}}$ 1.945				$\frac{P_{\text{ign}}}{10^{22} \text{ dyn cm}^{-2}}$ 2.24 ± 0.04
Number	M_{\odot}	km		MeV u ⁻¹	$10^{-9} M_{\odot} \text{ yr}^{-1}$	S	S	S	$10^{22} \rm dyn cm^{-2}$
Number 1	<i>M</i> _⊙	km 11.2	0.01	$\frac{\text{MeV u}^{-1}}{0.1}$	$10^{-9} M_{\odot} \text{ yr}^{-1}$ 1.945	$\frac{s}{6.08 \pm 0.53}$	s 22.37 \pm 2.57	$\frac{s}{40.34 \pm 3.46}$	$\frac{10^{22} \text{dyn cm}^{-2}}{2.24 \pm 0.04}$
Number 1 2	<i>M</i> _☉ 1.3 1.5	11.2 11.2	0.01 0.01	MeV u ⁻¹ 0.1 0.1	$\frac{10^{-9} M_{\odot} \text{ yr}^{-1}}{1.945}$ 1.945	$6.08 \pm 0.53 \\ 5.41 \pm 0.81$	$s \\ 22.37 \pm 2.57 \\ 15.26 \pm 2.41$	8	$\frac{10^{22} \text{ dyn cm}^{-2}}{2.24 \pm 0.04}$ 2.69 ± 0.08
Number 1 2 3	<i>M</i> _⊙ 1.3 1.5 1.7	11.2 11.2 11.2	0.01 0.01 0.01	0.1 0.1 0.1 0.1	$ \begin{array}{r} 10^{-9} M_{\odot} \text{ yr}^{-1} \\ \hline 1.945 \\ 1.945 \\ 1.945 \end{array} $	$ 6.08 \pm 0.53 $ $5.41 \pm 0.81 $ $4.42 \pm 0.81 $	s 22.37 ± 2.57 15.26 ± 2.41 10.97 ± 1.81	s 40.34 ± 3.46 28.43 ± 3.39 18.91 ± 2.42	$ \begin{array}{r} 10^{22} \text{dyn cm}^{-2} \\ \hline 2.24 \pm 0.04 \\ 2.69 \pm 0.08 \\ 3.46 \pm 0.13 \end{array} $
Number 1 2 3 4	<i>M</i> _⊙ 1.3 1.5 1.7 1.8	11.2 11.2 11.2 11.2	0.01 0.01 0.01 0.01	0.1 0.1 0.1 0.1 0.1	$ \begin{array}{r} 10^{-9} M_{\odot} \text{ yr}^{-1} \\ \hline 1.945 \\ 1.945 \\ 1.945 \\ 1.945 \end{array} $		s 22.37 ± 2.57 15.26 ± 2.41 10.97 ± 1.81 8.93 ± 0.65	$ 8 $ 40.34 ± 3.46 28.43 ± 3.39 18.91 ± 2.42 15.50 ± 0.99	$10^{22} \text{ dyn cm}^{-2}$ 2.24 ± 0.04 2.69 ± 0.08 3.46 ± 0.13 3.93 ± 0.10
Number 1 2 3 4 5	<i>M</i> _☉ 1.3 1.5 1.7 1.8 1.4	11.2 11.2 11.2 11.2 11.2	0.01 0.01 0.01 0.01 0.01	MeV u ⁻¹ 0.1 0.1 0.1 0.1 0.1 0.1	10 ⁻⁹ M _☉ yr ⁻¹ 1.945 1.945 1.945 1.945 1.945 1.945		s 22.37 ± 2.57 15.26 ± 2.41 10.97 ± 1.81 8.93 ± 0.65 16.84 ± 3.05	$\begin{array}{c} \text{s} \\ 40.34 \pm 3.46 \\ 28.43 \pm 3.39 \\ 18.91 \pm 2.42 \\ 15.50 \pm 0.99 \\ 31.53 \pm 4.03 \\ 42.55 \pm 4.74 \end{array}$	$10^{22} \text{ dyn cm}^{-2}$ 2.24 ± 0.04 2.69 ± 0.08 3.46 ± 0.13 3.93 ± 0.10 2.51 ± 0.08
Number 1 2 3 4 5 6	<i>M</i> _☉ 1.3 1.5 1.7 1.8 1.4 1.4	hm 11.2 11.2 11.2 11.2 11.2 11.2 11.2 12.0	0.01 0.01 0.01 0.01 0.01 0.01	MeV u ⁻¹ 0.1 0.1 0.1 0.1 0.1 0.1 0.1	10 ⁻⁹ M _☉ yr ⁻¹ 1.945 1.945 1.945 1.945 1.945 1.945 1.945	$\begin{array}{c} \text{s} \\ 6.08 \pm 0.53 \\ 5.41 \pm 0.81 \\ 4.42 \pm 0.81 \\ 4.55 \pm 0.33 \\ 5.62 \pm 0.69 \\ 6.32 \pm 0.64 \end{array}$	s 22.37 ± 2.57 15.26 ± 2.41 10.97 ± 1.81 8.93 ± 0.65 16.84 ± 3.05 22.57 ± 3.59	$\begin{array}{c} \text{s} \\ 40.34 \pm 3.46 \\ 28.43 \pm 3.39 \\ 18.91 \pm 2.42 \\ 15.50 \pm 0.99 \\ 31.53 \pm 4.03 \end{array}$	$10^{22} \text{ dyn cm}^{-2}$ 2.24 ± 0.04 2.69 ± 0.08 3.46 ± 0.13 3.93 ± 0.10 2.51 ± 0.08 2.12 ± 0.06
Number 1 2 3 4 5 6 7	<i>M</i> _⊙ 1.3 1.5 1.7 1.8 1.4 1.4	11.2 11.2 11.2 11.2 11.2 11.2 12.0 12.5	0.01 0.01 0.01 0.01 0.01 0.01 0.01	MeV u ⁻¹ 0.1 0.1 0.1 0.1 0.1 0.1 0.1 0.1 0.1	10 ⁻⁹ M _☉ yr ⁻¹ 1.945 1.945 1.945 1.945 1.945 1.945 1.945 1.945	$\begin{array}{c} \text{s} \\ 6.08 \pm 0.53 \\ 5.41 \pm 0.81 \\ 4.42 \pm 0.81 \\ 4.55 \pm 0.33 \\ 5.62 \pm 0.69 \\ 6.32 \pm 0.64 \\ 6.09 \pm 0.53 \end{array}$	$\begin{array}{c} \text{s} \\ 22.37 \pm 2.57 \\ 15.26 \pm 2.41 \\ 10.97 \pm 1.81 \\ 8.93 \pm 0.65 \\ 16.84 \pm 3.05 \\ 22.57 \pm 3.59 \\ 25.34 \pm 3.93 \end{array}$	$\begin{array}{c} \text{s} \\ 40.34 \pm 3.46 \\ 28.43 \pm 3.39 \\ 18.91 \pm 2.42 \\ 15.50 \pm 0.99 \\ 31.53 \pm 4.03 \\ 42.55 \pm 4.74 \\ 47.07 \pm 5.57 \end{array}$	$10^{22} \text{ dyn cm}^{-2}$ 2.24 ± 0.04 2.69 ± 0.08 3.46 ± 0.13 3.93 ± 0.10 2.51 ± 0.08 2.12 ± 0.06 1.89 ± 0.04
Number 1 2 3 4 5 6 7 8	<i>M</i> _⊙ 1.3 1.5 1.7 1.8 1.4 1.4 1.4 1.4	11.2 11.2 11.2 11.2 11.2 11.2 12.0 12.5 13.0	0.01 0.01 0.01 0.01 0.01 0.01 0.01	MeV u ⁻¹ 0.1 0.1 0.1 0.1 0.1 0.1 0.1 0	10 ⁻⁹ M _☉ yr ⁻¹ 1.945 1.945 1.945 1.945 1.945 1.945 1.945 1.945	$\begin{array}{c} \text{s} \\ 6.08 \pm 0.53 \\ 5.41 \pm 0.81 \\ 4.42 \pm 0.81 \\ 4.55 \pm 0.33 \\ 5.62 \pm 0.69 \\ 6.32 \pm 0.64 \\ 6.09 \pm 0.53 \\ 6.07 \pm 0.84 \\ \end{array}$	$\begin{array}{c} \text{s} \\ 22.37 \pm 2.57 \\ 15.26 \pm 2.41 \\ 10.97 \pm 1.81 \\ 8.93 \pm 0.65 \\ 16.84 \pm 3.05 \\ 22.57 \pm 3.59 \\ 25.34 \pm 3.93 \\ 25.88 \pm 6.16 \end{array}$	$\begin{array}{c} \text{s} \\ 40.34 \pm 3.46 \\ 28.43 \pm 3.39 \\ 18.91 \pm 2.42 \\ 15.50 \pm 0.99 \\ 31.53 \pm 4.03 \\ 42.55 \pm 4.74 \\ 47.07 \pm 5.57 \\ 47.90 \pm 10.51 \end{array}$	$10^{22} \text{ dyn cm}^{-2}$ 2.24 ± 0.04 2.69 ± 0.08 3.46 ± 0.13 3.93 ± 0.10 2.51 ± 0.08 2.12 ± 0.06 1.89 ± 0.04 1.75 ± 0.05
Number 1 2 3 4 5 6 7 8 9	<i>M</i> _☉ 1.3 1.5 1.7 1.8 1.4 1.4 1.4 1.4 1.4	11.2 11.2 11.2 11.2 11.2 11.2 12.0 12.5 13.0 11.2	0.01 0.01 0.01 0.01 0.01 0.01 0.01 0.01	MeV u ⁻¹ 0.1 0.1 0.1 0.1 0.1 0.1 0.1 0	10 ⁻⁹ M _☉ yr ⁻¹ 1.945 1.945 1.945 1.945 1.945 1.945 1.945 1.945 1.945	$\begin{array}{c} \text{s} \\ 6.08 \pm 0.53 \\ 5.41 \pm 0.81 \\ 4.42 \pm 0.81 \\ 4.55 \pm 0.33 \\ 5.62 \pm 0.69 \\ 6.32 \pm 0.64 \\ 6.09 \pm 0.53 \\ 6.07 \pm 0.84 \\ 5.27 \pm 0.86 \end{array}$	$\begin{array}{c} \text{s} \\ 22.37 \pm 2.57 \\ 15.26 \pm 2.41 \\ 10.97 \pm 1.81 \\ 8.93 \pm 0.65 \\ 16.84 \pm 3.05 \\ 22.57 \pm 3.59 \\ 25.34 \pm 3.93 \\ 25.88 \pm 6.16 \\ 14.54 \pm 3.57 \end{array}$	$\begin{array}{c} \text{s} \\ 40.34 \pm 3.46 \\ 28.43 \pm 3.39 \\ 18.91 \pm 2.42 \\ 15.50 \pm 0.99 \\ 31.53 \pm 4.03 \\ 42.55 \pm 4.74 \\ 47.07 \pm 5.57 \\ 47.90 \pm 10.51 \\ 24.91 \pm 5.35 \\ \end{array}$	$10^{22} \text{ dyn cm}^{-2}$ 2.24 ± 0.04 2.69 ± 0.08 3.46 ± 0.13 3.93 ± 0.10 2.51 ± 0.08 2.12 ± 0.06 1.89 ± 0.04 1.75 ± 0.05 2.30 ± 0.11
Number 1 2 3 4 5 6 7 8 9 10	<i>M</i> _☉ 1.3 1.5 1.7 1.8 1.4 1.4 1.4 1.4 1.4 1.4	11.2 11.2 11.2 11.2 11.2 11.2 12.0 12.5 13.0 11.2 11.2	0.01 0.01 0.01 0.01 0.01 0.01 0.01 0.02 0.02	MeV u ⁻¹ 0.1 0.1 0.1 0.1 0.1 0.1 0.1 0.1 0.1 0.	10 ⁻⁹ M _☉ yr ⁻¹ 1.945 1.945 1.945 1.945 1.945 1.945 1.945 1.945 1.945 1.945	$\begin{array}{c} \text{s} \\ 6.08 \pm 0.53 \\ 5.41 \pm 0.81 \\ 4.42 \pm 0.81 \\ 4.55 \pm 0.33 \\ 5.62 \pm 0.69 \\ 6.32 \pm 0.64 \\ 6.09 \pm 0.53 \\ 6.07 \pm 0.84 \\ 5.27 \pm 0.86 \\ 5.44 \pm 1.15 \end{array}$	$\begin{array}{c} \text{s} \\ 22.37 \pm 2.57 \\ 15.26 \pm 2.41 \\ 10.97 \pm 1.81 \\ 8.93 \pm 0.65 \\ 16.84 \pm 3.05 \\ 22.57 \pm 3.59 \\ 25.34 \pm 3.93 \\ 25.88 \pm 6.16 \\ 14.54 \pm 3.57 \\ 15.93 \pm 2.57 \\ \end{array}$	$\begin{array}{c} \text{s} \\ 40.34 \pm 3.46 \\ 28.43 \pm 3.39 \\ 18.91 \pm 2.42 \\ 15.50 \pm 0.99 \\ 31.53 \pm 4.03 \\ 42.55 \pm 4.74 \\ 47.07 \pm 5.57 \\ 47.90 \pm 10.51 \\ 24.91 \pm 5.35 \\ 28.73 \pm 2.97 \end{array}$	$10^{22} \text{ dyn cm}^{-2}$ 2.24 ± 0.04 2.69 ± 0.08 3.46 ± 0.13 3.93 ± 0.10 2.51 ± 0.08 2.12 ± 0.06 1.89 ± 0.04 1.75 ± 0.05 2.30 ± 0.11 2.12 ± 0.06
Number 1 2 3 4 5 6 7 8 9 10 11	<i>M</i> _☉ 1.3 1.5 1.7 1.8 1.4 1.4 1.4 1.4 1.4 1.4 1.4 1.4 1.4 1.4	11.2 11.2 11.2 11.2 11.2 12.0 12.5 13.0 11.2 11.2	0.01 0.01 0.01 0.01 0.01 0.01 0.01 0.02 0.02	MeV u ⁻¹ 0.1 0.1 0.1 0.1 0.1 0.1 0.1 0.1 0.1 0.	10 ⁻⁹ M _☉ yr ⁻¹ 1.945 1.945 1.945 1.945 1.945 1.945 1.945 1.945 1.945 1.945 1.945	$\begin{array}{c} s\\ 6.08\pm0.53\\ 5.41\pm0.81\\ 4.42\pm0.81\\ 4.55\pm0.33\\ 5.62\pm0.69\\ 6.32\pm0.64\\ 6.09\pm0.53\\ 6.07\pm0.84\\ 5.27\pm0.86\\ 5.44\pm1.15\\ 5.68\pm0.74 \end{array}$	$\begin{array}{c} s\\ 22.37 \pm 2.57\\ 15.26 \pm 2.41\\ 10.97 \pm 1.81\\ 8.93 \pm 0.65\\ 16.84 \pm 3.05\\ 22.57 \pm 3.59\\ 25.34 \pm 3.93\\ 25.88 \pm 6.16\\ 14.54 \pm 3.57\\ 15.93 \pm 2.57\\ 17.65 \pm 3.30\\ \end{array}$	$\begin{array}{c} \text{s} \\ 40.34 \pm 3.46 \\ 28.43 \pm 3.39 \\ 18.91 \pm 2.42 \\ 15.50 \pm 0.99 \\ 31.53 \pm 4.03 \\ 42.55 \pm 4.74 \\ 47.07 \pm 5.57 \\ 47.90 \pm 10.51 \\ 24.91 \pm 5.35 \\ 28.73 \pm 2.97 \\ 32.12 \pm 3.69 \end{array}$	$10^{22} \text{dyn cm}^{-2}$ 2.24 ± 0.04 2.69 ± 0.08 3.46 ± 0.13 3.93 ± 0.10 2.51 ± 0.08 2.12 ± 0.06 1.89 ± 0.04 1.75 ± 0.05 2.30 ± 0.11 2.12 ± 0.06 1.98 ± 0.04
Number 1 2 3 4 5 6 7 8 9 10 11 12	<i>M</i> _☉ 1.3 1.5 1.7 1.8 1.4 1.4 1.4 1.4 1.4 1.4 1.4 1.4 1.4 1.4	11.2 11.2 11.2 11.2 11.2 12.0 12.5 13.0 11.2 11.2 11.2	0.01 0.01 0.01 0.01 0.01 0.01 0.01 0.02 0.02	MeV u ⁻¹ 0.1 0.1 0.1 0.1 0.1 0.1 0.1 0.1 0.1 0.	10 ⁻⁹ M _☉ yr ⁻¹ 1.945 1.945 1.945 1.945 1.945 1.945 1.945 1.945 1.945 1.945 1.945 1.945	$\begin{array}{c} s\\ 6.08\pm0.53\\ 5.41\pm0.81\\ 4.42\pm0.81\\ 4.55\pm0.33\\ 5.62\pm0.69\\ 6.32\pm0.64\\ 6.09\pm0.53\\ 6.07\pm0.84\\ 5.27\pm0.86\\ 5.44\pm1.15\\ 5.68\pm0.74\\ 6.61\pm0.52\\ \end{array}$	$\begin{array}{c} s\\ 22.37 \pm 2.57\\ 15.26 \pm 2.41\\ 10.97 \pm 1.81\\ 8.93 \pm 0.65\\ 16.84 \pm 3.05\\ 22.57 \pm 3.59\\ 25.34 \pm 3.93\\ 25.88 \pm 6.16\\ 14.54 \pm 3.57\\ 15.93 \pm 2.57\\ 17.65 \pm 3.30\\ 19.06 \pm 4.55\\ \end{array}$	$\begin{array}{c} \text{s} \\ 40.34 \pm 3.46 \\ 28.43 \pm 3.39 \\ 18.91 \pm 2.42 \\ 15.50 \pm 0.99 \\ 31.53 \pm 4.03 \\ 42.55 \pm 4.74 \\ 47.07 \pm 5.57 \\ 47.90 \pm 10.51 \\ 24.91 \pm 5.35 \\ 28.73 \pm 2.97 \\ 32.12 \pm 3.69 \\ 36.82 \pm 6.84 \end{array}$	$10^{22} \text{dyn cm}^{-2}$ 2.24 ± 0.04 2.69 ± 0.08 3.46 ± 0.13 3.93 ± 0.10 2.51 ± 0.08 2.12 ± 0.06 1.89 ± 0.04 1.75 ± 0.05 2.30 ± 0.11 2.12 ± 0.06 1.98 ± 0.04 1.49 ± 0.03
Number 1 2 3 4 5 6 7 8 9 10 11 12 13	<i>M</i> _☉ 1.3 1.5 1.7 1.8 1.4 1.4 1.4 1.4 1.4 1.4 1.4 1.4 1.4 1.4	11.2 11.2 11.2 11.2 11.2 12.0 12.5 13.0 11.2 11.2 11.2 11.2	0.01 0.01 0.01 0.01 0.01 0.01 0.01 0.02 0.02	MeV u ⁻¹ 0.1 0.1 0.1 0.1 0.1 0.1 0.1 0.1 0.1 0.	10 ⁻⁹ M _☉ yr ⁻¹ 1.945 1.945 1.945 1.945 1.945 1.945 1.945 1.945 1.945 1.945 1.945 1.945 1.945 2.0	$\begin{array}{c} s\\ 6.08\pm0.53\\ 5.41\pm0.81\\ 4.42\pm0.81\\ 4.55\pm0.33\\ 5.62\pm0.69\\ 6.32\pm0.64\\ 6.09\pm0.53\\ 6.07\pm0.84\\ 5.27\pm0.86\\ 5.44\pm1.15\\ 5.68\pm0.74\\ 6.61\pm0.52\\ 6.16\pm0.63\\ \end{array}$	$\begin{array}{c} s\\ 22.37 \pm 2.57\\ 15.26 \pm 2.41\\ 10.97 \pm 1.81\\ 8.93 \pm 0.65\\ 16.84 \pm 3.05\\ 22.57 \pm 3.59\\ 25.34 \pm 3.93\\ 25.88 \pm 6.16\\ 14.54 \pm 3.57\\ 15.93 \pm 2.57\\ 17.65 \pm 3.30\\ 19.06 \pm 4.55\\ 17.61 \pm 3.87\\ \end{array}$	$\begin{array}{c} s\\ 40.34 \pm 3.46\\ 28.43 \pm 3.39\\ 18.91 \pm 2.42\\ 15.50 \pm 0.99\\ 31.53 \pm 4.03\\ 42.55 \pm 4.74\\ 47.07 \pm 5.57\\ 47.90 \pm 10.51\\ 24.91 \pm 5.35\\ 28.73 \pm 2.97\\ 32.12 \pm 3.69\\ 36.82 \pm 6.84\\ 33.12 \pm 5.54\\ \end{array}$	$10^{22} \text{dyn cm}^{-2}$ 2.24 ± 0.04 2.69 ± 0.08 3.46 ± 0.13 3.93 ± 0.10 2.51 ± 0.08 2.12 ± 0.06 1.89 ± 0.04 1.75 ± 0.05 2.30 ± 0.11 2.12 ± 0.06 1.98 ± 0.04 1.49 ± 0.03 1.75 ± 0.03
Number 1 2 3 4 5 6 7 8 9 10 11 12 13 14	<i>M</i> _☉ 1.3 1.5 1.7 1.8 1.4 1.4 1.4 1.4 1.4 1.4 1.4 1.4 1.4 1.4	11.2 11.2 11.2 11.2 11.2 12.0 12.5 13.0 11.2 11.2 11.2 11.2 11.601 11.601	0.01 0.01 0.01 0.01 0.01 0.01 0.01 0.02 0.02 0.02 0.02 0.02 0.02	MeV u ⁻¹ 0.1 0.1 0.1 0.1 0.1 0.1 0.1 0	10 ⁻⁹ M _☉ yr ⁻¹ 1.945 1.945 1.945 1.945 1.945 1.945 1.945 1.945 1.945 1.945 1.945 1.945 1.945 2.0 2.5	$\begin{array}{c} s\\ 6.08\pm0.53\\ 5.41\pm0.81\\ 4.42\pm0.81\\ 4.55\pm0.33\\ 5.62\pm0.69\\ 6.32\pm0.64\\ 6.09\pm0.53\\ 6.07\pm0.84\\ 5.27\pm0.86\\ 5.44\pm1.15\\ 5.68\pm0.74\\ 6.61\pm0.52\\ 6.16\pm0.63\\ 6.51\pm0.59 \end{array}$	$\begin{array}{c} s\\ 22.37 \pm 2.57\\ 15.26 \pm 2.41\\ 10.97 \pm 1.81\\ 8.93 \pm 0.65\\ 16.84 \pm 3.05\\ 22.57 \pm 3.59\\ 25.34 \pm 3.93\\ 25.88 \pm 6.16\\ 14.54 \pm 3.57\\ 15.93 \pm 2.57\\ 17.65 \pm 3.30\\ 19.06 \pm 4.55\\ 17.61 \pm 3.87\\ 17.83 \pm 3.32\\ \end{array}$	$\begin{array}{c} s\\ 40.34 \pm 3.46\\ 28.43 \pm 3.39\\ 18.91 \pm 2.42\\ 15.50 \pm 0.99\\ 31.53 \pm 4.03\\ 42.55 \pm 4.74\\ 47.07 \pm 5.57\\ 47.90 \pm 10.51\\ 24.91 \pm 5.35\\ 28.73 \pm 2.97\\ 32.12 \pm 3.69\\ 36.82 \pm 6.84\\ 33.12 \pm 5.54\\ 32.70 \pm 5.44\\ \end{array}$	$10^{22} \text{dyn cm}^{-2}$ 2.24 ± 0.04 2.69 ± 0.08 3.46 ± 0.13 3.93 ± 0.10 2.51 ± 0.08 2.12 ± 0.06 1.89 ± 0.04 1.75 ± 0.05 2.30 ± 0.11 2.12 ± 0.06 1.98 ± 0.04 1.49 ± 0.03 1.75 ± 0.03 1.84 ± 0.06
Number 1 2 3 4 5 6 7 8 9 10 11 12 13 14 15	<i>M</i> _☉ 1.3 1.5 1.7 1.8 1.4 1.4 1.4 1.4 1.4 1.4 1.4 1.4 1.4 1.4	hm 11.2 11.2 11.2 11.2 11.2 11.2 12.0 12.5 13.0 11.2 11.2 11.2 11.601 11.601 11.601	0.01 0.01 0.01 0.01 0.01 0.01 0.01 0.02 0.02 0.02 0.02 0.02 0.02 0.02	MeV u ⁻¹ 0.1 0.1 0.1 0.1 0.1 0.1 0.1 0	10 ⁻⁹ M _☉ yr ⁻¹ 1.945	$\begin{array}{c} s\\ 6.08\pm0.53\\ 5.41\pm0.81\\ 4.42\pm0.81\\ 4.55\pm0.33\\ 5.62\pm0.69\\ 6.32\pm0.64\\ 6.09\pm0.53\\ 6.07\pm0.84\\ 5.27\pm0.86\\ 5.44\pm1.15\\ 5.68\pm0.74\\ 6.61\pm0.52\\ 6.16\pm0.63\\ 6.51\pm0.59\\ 6.33\pm0.63\\ \end{array}$	$\begin{array}{c} & & \\ 22.37 \pm 2.57 \\ 15.26 \pm 2.41 \\ 10.97 \pm 1.81 \\ 8.93 \pm 0.65 \\ 16.84 \pm 3.05 \\ 22.57 \pm 3.59 \\ 25.34 \pm 3.93 \\ 25.88 \pm 6.16 \\ 14.54 \pm 3.57 \\ 15.93 \pm 2.57 \\ 17.65 \pm 3.30 \\ 19.06 \pm 4.55 \\ 17.61 \pm 3.87 \\ 17.83 \pm 3.32 \\ 18.96 \pm 4.38 \\ \end{array}$	$\begin{array}{c} s\\ 40.34 \pm 3.46\\ 28.43 \pm 3.39\\ 18.91 \pm 2.42\\ 15.50 \pm 0.99\\ 31.53 \pm 4.03\\ 42.55 \pm 4.74\\ 47.07 \pm 5.57\\ 47.90 \pm 10.51\\ 24.91 \pm 5.35\\ 28.73 \pm 2.97\\ 32.12 \pm 3.69\\ 36.82 \pm 6.84\\ 33.12 \pm 5.54\\ 32.70 \pm 5.44\\ 35.73 \pm 6.80\\ \end{array}$	$10^{22} \text{dyn cm}^{-2}$ 2.24 ± 0.04 2.69 ± 0.08 3.46 ± 0.13 3.93 ± 0.10 2.51 ± 0.08 2.12 ± 0.06 1.89 ± 0.04 1.75 ± 0.03 1.21 ± 0.03 1.75 ± 0.03 1.84 ± 0.06 1.90 ± 0.08 2.03 ± 0.10
Number 1 2 3 4 5 6 7 8 9 10 11 12 13 14 15 16	<i>M</i> _⊙ 1.3 1.5 1.7 1.8 1.4 1.4 1.4 1.4 1.4 1.4 1.4 1.4 1.4 1.4	hm 11.2 11.2 11.2 11.2 11.2 11.2 12.0 12.5 13.0 11.2 11.2 11.2 11.601 11.601 11.601 11.601	0.01 0.01 0.01 0.01 0.01 0.01 0.01 0.02 0.02 0.02 0.02 0.02 0.02 0.02 0.02	MeV u ⁻¹ 0.1 0.1 0.1 0.1 0.1 0.1 0.1 0	10 ⁻⁹ M _☉ yr ⁻¹ 1.945	$\begin{array}{c} s\\ 6.08 \pm 0.53\\ 5.41 \pm 0.81\\ 4.42 \pm 0.81\\ 4.55 \pm 0.33\\ 5.62 \pm 0.69\\ 6.32 \pm 0.64\\ 6.09 \pm 0.53\\ 6.07 \pm 0.84\\ 5.27 \pm 0.86\\ 5.44 \pm 1.15\\ 5.68 \pm 0.74\\ 6.61 \pm 0.52\\ 6.16 \pm 0.63\\ 6.51 \pm 0.59\\ 6.33 \pm 0.63\\ 6.48 \pm 0.66\\ \end{array}$	$\begin{array}{c} s\\ 22.37 \pm 2.57\\ 15.26 \pm 2.41\\ 10.97 \pm 1.81\\ 8.93 \pm 0.65\\ 16.84 \pm 3.05\\ 22.57 \pm 3.59\\ 25.34 \pm 3.93\\ 25.88 \pm 6.16\\ 14.54 \pm 3.57\\ 15.93 \pm 2.57\\ 17.65 \pm 3.30\\ 19.06 \pm 4.55\\ 17.61 \pm 3.87\\ 17.83 \pm 3.32\\ 18.96 \pm 4.38\\ 18.13 \pm 4.13\\ \end{array}$	$\begin{array}{c} s\\ 40.34 \pm 3.46\\ 28.43 \pm 3.39\\ 18.91 \pm 2.42\\ 15.50 \pm 0.99\\ 31.53 \pm 4.03\\ 42.55 \pm 4.74\\ 47.07 \pm 5.57\\ 47.90 \pm 10.51\\ 24.91 \pm 5.35\\ 28.73 \pm 2.97\\ 32.12 \pm 3.69\\ 36.82 \pm 6.84\\ 33.12 \pm 5.54\\ 32.70 \pm 5.44\\ 35.73 \pm 6.80\\ 33.32 \pm 7.03\\ \end{array}$	$10^{22} \text{dyn cm}^{-2}$ 2.24 ± 0.04 2.69 ± 0.08 3.46 ± 0.13 3.93 ± 0.10 2.51 ± 0.08 2.12 ± 0.06 1.89 ± 0.04 1.75 ± 0.03 1.98 ± 0.04 1.49 ± 0.03 1.75 ± 0.03 1.84 ± 0.06 1.90 ± 0.08
Number 1 2 3 4 5 6 7 8 9 10 11 12 13 14 15 16 17	<i>M</i> _☉ 1.3 1.5 1.7 1.8 1.4 1.4 1.4 1.4 1.4 1.4 1.4 1.4 1.4 1.4	hm 11.2 11.2 11.2 11.2 11.2 11.2 12.0 12.5 13.0 11.2 11.2 11.2 11.601 11.601 11.601 11.601 11.601	0.01 0.01 0.01 0.01 0.01 0.01 0.01 0.02 0.02 0.02 0.02 0.02 0.02 0.02 0.02 0.02	MeV u ⁻¹ 0.1 0.1 0.1 0.1 0.1 0.1 0.1 0	10 ⁻⁹ M _☉ yr ⁻¹ 1.945 2.0 2.5 3.0 4.0 2.5	$\begin{array}{c} s\\ 6.08\pm0.53\\ 5.41\pm0.81\\ 4.42\pm0.81\\ 4.55\pm0.33\\ 5.62\pm0.69\\ 6.32\pm0.64\\ 6.09\pm0.53\\ 6.07\pm0.84\\ 5.27\pm0.86\\ 5.44\pm1.15\\ 5.68\pm0.74\\ 6.61\pm0.52\\ 6.16\pm0.63\\ 6.51\pm0.59\\ 6.33\pm0.63\\ 6.48\pm0.66\\ 6.44\pm0.70\\ \end{array}$	$\begin{array}{c} & & \\ 22.37 \pm 2.57 \\ 15.26 \pm 2.41 \\ 10.97 \pm 1.81 \\ 8.93 \pm 0.65 \\ 16.84 \pm 3.05 \\ 22.57 \pm 3.59 \\ 25.34 \pm 3.93 \\ 25.88 \pm 6.16 \\ 14.54 \pm 3.57 \\ 15.93 \pm 2.57 \\ 17.65 \pm 3.30 \\ 19.06 \pm 4.55 \\ 17.61 \pm 3.87 \\ 17.83 \pm 3.32 \\ 18.96 \pm 4.38 \\ 18.13 \pm 4.13 \\ 19.16 \pm 3.7 \\ \end{array}$	$\begin{array}{c} s\\ 40.34 \pm 3.46\\ 28.43 \pm 3.39\\ 18.91 \pm 2.42\\ 15.50 \pm 0.99\\ 31.53 \pm 4.03\\ 42.55 \pm 4.74\\ 47.07 \pm 5.57\\ 47.90 \pm 10.51\\ 24.91 \pm 5.35\\ 28.73 \pm 2.97\\ 32.12 \pm 3.69\\ 36.82 \pm 6.84\\ 33.12 \pm 5.54\\ 32.70 \pm 5.44\\ 35.73 \pm 6.80\\ 33.32 \pm 7.03\\ 36.04 \pm 4.96\\ \end{array}$	$10^{22} \text{dyn cm}^{-2}$ 2.24 ± 0.04 2.69 ± 0.08 3.46 ± 0.13 3.93 ± 0.10 2.51 ± 0.08 2.12 ± 0.06 1.89 ± 0.04 1.75 ± 0.03 1.21 ± 0.03 1.75 ± 0.03 1.84 ± 0.06 1.90 ± 0.08 2.03 ± 0.10 2.08 ± 0.06

Note. Errors of output parameters indicate the 1σ standard deviation.

EOS	$M \over M_{\odot}$	R km	$Z_{ m CNO}$	$10^{-9} \frac{\dot{M}}{M_{\odot}} \mathrm{yr}^{-1}$	α	τ s	Δt hr	$E_{ m burst}$ $10^{39} { m erg}$	$\frac{L_{\text{peak}}}{10^{38} \text{ erg s}^{-1}}$	t _{rise} S	τ _e s
Togashi	1.4	11.601	0.02	2.0	57.28 ± 1.44	27.89 ± 1.81	3.04 ± 0.07	4.28 ± 0.08	1.54 ± 0.10	5.15 ± 0.44	19.55 ± 2.07
Togashi	1.4	11.601	0.02	2.5	53.11 ± 1.77	39.14 ± 2.06	2.17 ± 0.06	4.12 ± 0.09	1.06 ± 0.07	4.41 ± 0.50	29.19 ± 1.89
Togashi	1.4	11.601	0.02	3.0	52.73 ± 2.11	42.22 ± 2.23	1.76 ± 0.05	4.05 ± 0.12	0.96 ± 0.08	4.09 ± 0.48	30.79 ± 1.94
Togashi	1.4	11.601	0.02	4.0	52.10 ± 1.08	46.39 ± 1.22	1.27 ± 0.02	3.93 ± 0.08	0.85 ± 0.03	4.03 ± 0.31	34.00 ± 1.87

Note. The base heat calculated from the luminosity value on the crust surface is $Q_b = 0.35$ MeV u⁻¹ (Dohi et al. 2021). The data are different from Dohi et al. (2021) in that the adopted reaction rates of 64 Ge(p, γ) 65 As and 65 As(p, γ) 66 Se are from Cyburt et al. (2016) for the former and Lam et al. (2016) for latter.

Table 3

Nuclear Reaction Network of rp.net (304 Species) and APRX3 (88 Species)

	rp.net	APRX3		rp.net	APRX3		rp.net	APRX3		rp.net	APRX3	
Z = 1-13	A		Z = 14-26	A		Z = 27-39		A	Z = 40-52		\boldsymbol{A}	
Н	1–3	1	Si	24-30	24–25	Co	51–57		Zr	78–83	80, 84	
He	3, 4	4	P	26-31		Ni	52-56	54, 56, 60	Nb	81-85	88	
Li	7		S	27-34	28-30	Cu	54-63		Mo	82-86	84	
Be	7, 8		Cl	30-35		Zn	55-66	60, 64	Tc	85-88	92	
В	8, 11		Ar	31-38	33-34	Ga	59-67		Ru	86-91	88, 90, 92	
C	9, 11, 12	12	K	35-39		Ge	60-68	62-64, 68	Rh	89-93	96	
N	12-15		Ca	36-44	37-40	As	64-69		Pd	90-94	92, 94, 96, 98	
O	13-18	14-16	Sc	39-45		Se	65-72	68, 72	Ag	94-98	97-98, 102	
F	17-19		Ti	40-47	42	Br	68-73		Cd	95-99	102-106	
Ne	18-21	18	V	43-49		Kr	69-74	72, 76	In	98-104	99, 102-107, 109	
Na	20-23		Cr	44-52	46	Rb	73-77		Sn	99-105	100-109, 112	
Mg	21-25	21-22	Mn	47-53		Sr	74-78	76, 80	Sb	106	106–108	
Al	22-27		Fe	48-56	48, 50	Y	77-82		Te	107	107-109	

Note. Nuclear reaction grids from Lund Fisker et al. (2007) and Dohi et al. (2020), respectively.

ORCID iDs

Helei Liu (刘荷蕾) ⓑ https://orcid.org/0000-0001-8706-1882 Akira Dohi (土肥明) ⓑ https://orcid.org/0000-0001-8726-5762

Nobuya Nishimura (西 村信哉) ® https://orcid.org/0000-0002-0842-7856

Weiyang Wang (王维扬) ® https://orcid.org/0000-0001-9036-8543

Renxin Xu (徐仁新) ¹⁰ https://orcid.org/0000-0002 -9042-3044

References

Abbott, B. P., Abbott, R., Abbott, T. D., et al. 2018, PhRvL, 121, 161101 Asplund, M., Grevesse, N., Sauval, A. J., & Scott, P. 2009, ARA&A, 47, 481 Ayasli, S., & Joss, P. C. 1982, ApJ, 256, 637 Belian, R. D., Conner, J. P., & Evans, W. D. 1976, ApJL, 206, L135

Bildsten, L. 1998, in The Many Faces of Neutron Stars, ed. R. Buccheri, J. van Paradijs, & A. Alpar, Vol. 515 (Dordrecht: Kluwer), 419

Bildsten, L. 2000, in AIP Conf. Ser. 522, Cosmic Explosions: Tenth AstroPhysics Conf., ed. S. S. Holt & W. W. Zhang (Melville, NY: AIP), 359

Brown, E. F. 2000, ApJ, 531, 988

Brown, E. F. 2015, dStar: Neutron star thermal evolution code, Astrophysics Source Code Library, ascl:1505.034

Brown, E. F., Bildsten, L., & Chang, P. 2002, ApJ, 574, 920

Brown, E. F., & Cumming, A. 2009, ApJ, 698, 1020

Colpi, M., Geppert, U., Page, D., & Possenti, A. 2001, ApJL, 548, L175

Cromartie, H. T., Fonseca, E., Ransom, S. M., et al. 2020, NatAs, 4, 72

Cumming, A., & Macbeth, J. 2006, ApJ, 646, 429

Cyburt, R. H., Amthor, A. M., Ferguson, R., et al. 2010, ApJS, 189, 240

Cyburt, R. H., Amthor, A. M., Heger, A., et al. 2016, ApJ, 830, 55

Deibel, A., Cumming, A., Brown, E. F., & Page, D. 2015, ApJL, 809, L31 Deibel, A., Cumming, A., Brown, E. F., & Reddy, S. 2017, ApJ, 839, 95

Deibel, A., Meisel, Z., Schatz, H., et al. 2016, ApJ, 831, 13

Dohi, A., Hashimoto, M.-a., Yamada, R., et al. 2020, PTEP, 2020, 033E02

Dohi, A., Nakazato, K., Hashimoto, M.-a., et al. 2019, PTEP, 2019, 113E01

Dohi, A., Nishimura, N., Hashimoto, M., et al. 2021, ApJ, 923, 64

Dohi, A., Nishimura, N., Sotani, H., et al. 2022, ApJ, 937, 124

Fisker, J. L. 2005, PhD thesis, Univ. Basel

Fisker, J. L., Görres, J., Wiescher, M., & Davids, B. 2006, ApJ, 650, 332

Fisker, J. L., Tan, W., Görres, J., et al. 2007, ApJ, 665, 637

Fujimoto, M. Y., Hanawa, T., Iben, I., & Richardson, M. B, J. 1984, ApJ, 278, 813

Galloway, D. K., & Keek, L. 2021, in Timing Neutron Stars: Pulsations, Oscillations and Explosions, ed. T. M. Belloni, M. Méndez, & C. Zhang, Vol. 461 (Berlin: Springer), 209

Galloway, D. K., Muno, M. P., Hartman, J. M., et al. 2008, ApJS, 179, 360

```
Galloway, D. K., Zand, J., & Chenevez, J. 2020, J, ApJS, 249, 32
Grevesse, N., & Sauval, A. J. 1998, SSRv, 85, 161
Grindlay, J., Gursky, H., Schnopper, H., et al. 1976, ApJL, 205, L127
Haensel, P. 2003, A&A, 404, L33
Haensel, P. 2008, A&A, 480, 459
Haensel, P., & Zdunik, J. L. 1990, A&A, 227, 431
Heger, A., Cumming, A., Galloway, D. K., & Woosley, S. E. 2007, ApJL,
Jermyn, A. S., Schwab, J., Bauer, E., et al. 2021, ApJ, 913, 72
Johnston, Z., Heger, A., & Galloway, D. K. 2018, MNRAS, 477, 2112
Johnston, Z., Heger, A., & Galloway, D. K. 2020, MNRAS, 494, 4576
José, J., & Hernanz, M. 1998, ApJ, 494, 680
José, J., Moreno, F., Parikh, A., & Iliadis, C. 2010, ApJS, 189, 204
Joss, P. C. 1977, Natur, 270, 310
Joss, P. C., & Li, F. K. 1980, ApJ, 238, 287
Keek, L., & Heger, A. 2011, ApJ, 743, 189
Keek, L., & Heger, A. 2016, MNRAS, 456, L11
Keek, L., & Heger, A. 2017, ApJ, 842, 113
Lam, Y. H., He, J. J., Parikh, A., et al. 2016, ApJ, 818, 78
Lewin, W. H. G., van Paradijs, J., & Taam, R. E. 1993, SSRv, 62, 223
Liebendörfer, M., Rosswog, S., & Thielemann, F.-K. 2002, ApJS, 141, 229
Liu, H., & Dohi, A. 2021, PhRvD, 103, 063009
Lu, X.-Y., Lü, G.-L., Liu, H.-L., et al. 2022, RAA, 22, 055018
Lund Fisker, J., Schatz, H., & Thielemann, F.-K. 2007, ApJS, 174, 261
Matsuo, Y., Liu, H., Hashimoto, M.-A., & Noda, T. 2018, Limpe, 27, 1850067
Meisel, Z. 2018, ApJ, 860, 147
Meisel, Z., & Deibel, A. 2017, ApJ, 837, 73
Meisel, Z., Merz, G., & Medvid, S. 2019, ApJ, 872, 84
Page, D., & Reddy, S. 2013, PhRvL, 111, 241102
Page, D. P. 1989, PhD thesis, SUNY Stony Brook, New York
Parikh, A., José, J., Moreno, F., & Iliadis, C. 2008, ApJS, 178, 110
Parikh, A., José, J., Sala, G., & Iliadis, C. 2013, PrPNP, 69, 225
Paxton, B., Bildsten, L., Dotter, A., et al. 2011, ApJS, 192, 3
Paxton, B., Cantiello, M., Arras, P., et al. 2013, ApJS, 208, 4
Paxton, B., Marchant, P., Schwab, J., et al. 2015, ApJS, 220, 15
Paxton, B., Schwab, J., Bauer, E. B., et al. 2018, ApJS, 234, 34
Potekhin, A. Y., & Chabrier, G. 2010, CoPP, 50, 82
Potekhin, A. Y., & Chabrier, G. 2018, A&A, 609, A74
Potekhin, A. Y., & Chabrier, G. 2021, A&A, 645, A102
Rogers, F. J., & Nayfonov, A. 2002, ApJ, 576, 1064
Saumon, D., Chabrier, G., & van Horn, H. M. 1995, ApJS, 99, 713
Schatz, H., Gupta, S., Möller, P., et al. 2014, Natur, 505, 62
Steiner, A. W., Lattimer, J. M., & Brown, E. F. 2010, ApJ, 722, 33
Taam, R. E. 1980, ApJ, 241, 358
Taam, R. E. 1985, ARNPS, 35, 1
Timmes, F. X., & Swesty, F. D. 2000, ApJS, 126, 501
Togashi, H., Nakazato, K., Takehara, Y., et al. 2017, NuPhA, 961, 78
Ubertini, P., Bazzano, A., Cocchi, M., et al. 1999, ApJL, 514, L27
Wallace, R. K., & Woosley, S. E. 1981, ApJS, 45, 389
```

Woosley, S. E., Heger, A., Cumming, A., et al. 2004, ApJS, 151, 75

Woosley, S. E., & Taam, R. E. 1976, Natur, 263, 101